THE PENNSYLVANIA STATE UNIVERSITY
SCHREYER HONORS COLLEGE

DEPARTMENT OF MECHANICAL AND NUCLEAR ENGINEERING

MIMICKING NATURE'S MECHANISMS: CREATING A DIRECTIONALLY OMNIPHOBIC LIQUID INFUSED SURFACE COATING

JONATHAN WANG
SPRING 2014

A thesis
submitted in partial fulfillment
of the requirements
for a baccalaureate degree
in Mechanical Engineering
with honors in Mechanical Engineering

Reviewed and approved* by the following:

Tak-Sing Wong
Assistant Professor of Mechanical Engineering
Thesis Supervisor

Domenic Santavicca
Professor of Mechanical Engineering
Honors Adviser

* Signatures are on file in the Schreyer Honors College.

ABSTRACT

Nature is often the inspiration for new emerging technology today. In particular, several species of plant and animal life use structured surfaces to directionally transfer liquids. A butterfly's hydrophobic wings are structured so that water is directionally repelled away from the body. The *Nepenthes* pitcher plant exhibits a structured surface that when wetted, can repel various liquids and null the adhesive forces used by insects to scale walls. In this thesis, these two mechanisms were combined into one synthetic surface which aimed to directionally repel various liquids of differing surface tensions. Four microgrooved surfaces of differing groove dimensions were created for testing. To test the effectiveness of these directional surfaces, the height of the lubricant used to coat the surfaces and produce a thin film was measured at various spin coating speeds. The surface samples were then tested with an inclinometer to measure the sliding angle difference between the parallel and perpendicular orientations at the corresponding spin speed and lubricant height. With this data, it was concluded that the directional surfaces showed significant ability to directionally repel water, hexadecane, and octane test droplets. Some potential further work is then discussed which could help explain any discrepancies within the test data.

TABLE OF CONTENTS

LIST OF FIGURES

LIST OF TABLES

ACKNOWLEDGEMENTS

First, I would like to thank Dr. Tak-Sing Wong for allowing me to work with his research group for this thesis. Thank you for the guidance in both the research itself as well as the writing of this report. I would also like to thank Jing Wang for helping me every step of the way through all the work that needed to be done in the lab. I learned a lot this past year from you all. Lastly, I would like to thank Dr. Domenic Santavicca for getting me connected with Dr. Wong in the first place, and for all the help and advice you've had for me regarding this thesis and other subjects over the past four years.

Chapter 1

Introduction

Inspiration

Natural mechanisms found in Earth's plant and animal are often much more highly complex than they appear to the casual observer. Many of these mechanisms can be extremely useful to the human population if they can be imitated and understood correctly. That is why many researchers across the world have published works regarding the testing of natural mechanisms to better understand how they work, and to hopefully apply those same principles to relevant human technology. One particular natural mechanism that can be seen in different species is a mechanism for directional water collection or repellence.

First, we examine the mechanisms driving fog collection in cacti, particularly of the species *O. microdasys*. In a study done for *Nature Communications*, researchers experimented with this cactus species to determine how it uses its barbs to directionally collect water droplets from fog. After initial testing, they observed that water droplets moved directionally from the tip of the barbs toward the base, no matter what orientation the barbs were at. This even held true for barbs oriented vertically, so that the water droplets had to move against the force of gravity. Eventually, the researchers were able to model this water collection mechanism as a product of two driving forces: one from a Laplace pressure gradient and one from a surface roughness gradient. They found that

due to the conical shape of the barbs, a pressure gradient is formed so that a water droplet is forced toward the end of larger radius. They also found that the barbs of the cactus are naturally structured with microgrooves. These microgrooves have a width gradient due to the conical shape of the barbs. This intrinsically creates a roughness gradient in which the barbs are rougher near the point than the base. This in turn creates a gradient of surface free energy which becomes the second driving force behind the water droplets (Ju et al.).

Next, we examine the directional water collection exhibited by spider silk. In an article published by *Nature*, researchers studied the water collection mechanism of cribellate spider silk. It was first observed that cribellate spiders are able to separate their silk into much finer, hydrophilic nanofibrils. These fibers greatly enhance the wettability of the silk, and help the silk to condense water from humid air. The original, dry structure of the spider silk can be seen in Figure 1. The silk is structured as a pattern of puffs and joints of the nanofibrils. As water condenses on the silk, the structure slowly changes. Each puff becomes gradually smaller until a pattern of small spindle-knots is formed. Water continues to condense on the silk, and eventually the droplets begin to move toward the spindle knots. This phenomenon can be explained in the same manner as the directional collection of water in cacti. The spindle knots (see Figure 1) are essentially cones of spider silk fibers. The conical shape again presents a Laplace pressure gradient that helps to drive the droplets toward a higher radius. Since the silk is made up of countless individual nanofibers, at the micro level, the silk is effectively grooved. The microgrooves of the fibers then create a gradient of surface free energy just as in the cactus barbs. The force from this gradient along with the pressure force pushes the water droplets away from the joints, and toward the spindle knots (Zheng et al.).

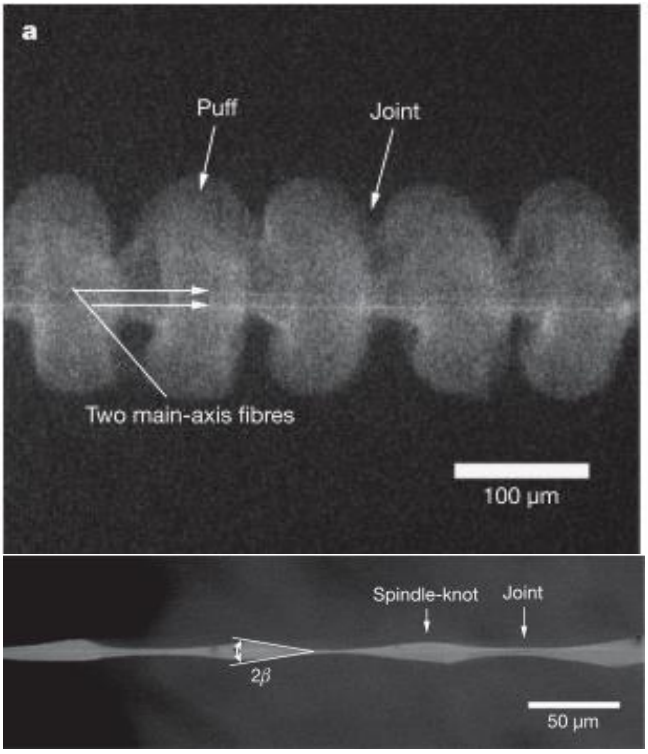

Figure 1: Top: dry structure of spider web. Bottom: spindle knots after after water condensation. Reprinted by permission from Macmillan Publishers Ltd: [*Nature*] (Zheng et al.), copyright (2007)

Perhaps the most important example of directional water transfer in nature is with the wings of a butterfly. Butterfly wings have a nanostructure comprised of flexible, stacked nanostrips atop overlapped scales. This structure allows the wings to exhibit superhydrophobicity when they are tilted downward. This is because the overlapping of the strips keeps contact between the water and the nanostrips minimal. Air pockets are formed in the grooves of the scales and an essentially Cassie wetting regime is seen. When the wings are tilted upward, water droplets experience more contact area with the surface. This represents an intermediate state between the Cassie and Wenzel regimes as there is still some air trapped beneath the water. This increased contact area creates a high energy barrier and the droplet tightly adheres to the wing surface rather than slipping off

of it. Thus, overall the structure of the butterfly wing stops water from rolling in toward the body and allows droplets to easily roll of in the outward direction. The Cassie and Wenzel models of wetting will be discussed further in Chapter 4 (Zheng, Gao, and Jiang).

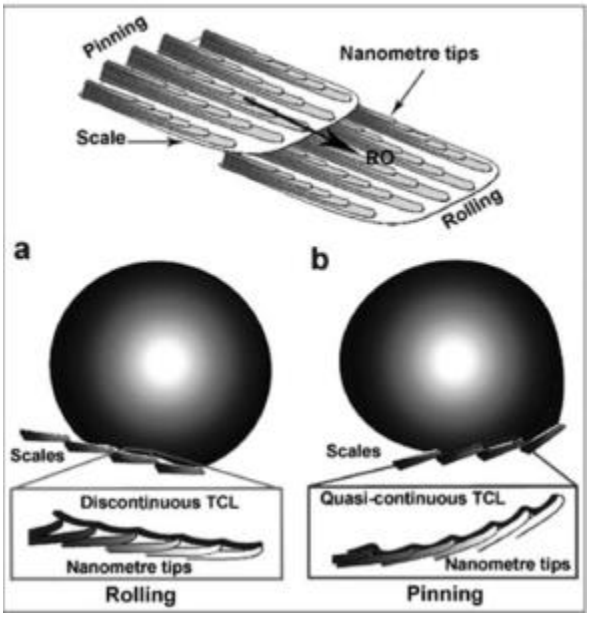

Figure 2: Butterfly wing nanostructure. Notice the geometry of the contact line in both the rolling and the pinning case. The flexible nanostrips play a key part in the varying contact areas Reproduced from (Zheng, Gao, and Jiang) with permission of the Royal Society of Chemistry

While structures like the one seen in butterfly wings is effective in repelling water, a structure alone would not be as effective in repelling liquids of varying surface tension. The *Nepenthes* pitcher plant employs a mechanism in which omniphobicity is induced on its surface in order to catch prey. The surface is comprised of an anisotropic arrangement of overlapping cells, which allows for increased wettability. The pitcher plant surface can then be fully wetted by rain water or a nectar produced by the plant. This forms a homogeneous liquid film that prevents insects from adhering to the plant

surface. This film, while not capable of directional repellency, is able to repel a variety of different liquids and solids (Scholz et al.).

Related Work and Purpose

Research done by Dr. Tak-Sing Wong et al has already produced a surface that exhibits omniphobicity. The surface, called a slippery liquid-infused porous surface (SLIPS), was successful in repelling both high and low surface tension liquids. In all, two different SLIPS surfaces were created, and both exhibited very low contact angle hysteresis of less than 2.5° and low sliding angles of less than 5°. Both SLIPS were made omniphobic by lubricants wicking into and wetting the porous structures. Figure 3 shows the effectiveness of the SLIPS in repelling blood as compared to other surfaces. It is clear that the SLIPS is highly successful in completely repelling the liquid while the other surfaces do not. With more research, it is anticipated that SLIPS can have a broad impact in biomedical fluid handling, anti-icing, fuel transport, and more (Wong et al.).

Another surface created by Pengchao Zhang et al exhibited the anisotropic sliding of water droplets which this work seeks to imitate. Zhang et al used a poly(butyl methacrylate-co-lauryl methacrylate) organogel surface in combination with silicone oil to achieve this. The surface had structured periodic microgrooves as shown in Figure 4. At an angle of 10° (using a sample with a groove width of 80 microns), it was recorded that a 5 mg droplet of water easily slid in the direction parallel to the grooves. However, when tilted in the perpendicular direction, the droplet was pinned to the surface. This can

be attributed to the fact that the droplet experienced a Wenzel state in the microgrooves and was therefore significantly impeded in this direction (Zhang et al.).

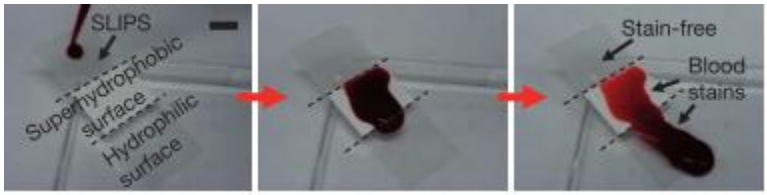

Figure 3: Effectiveness of SLIPS in repelling blood as compared to a superhydrophobic surface and a hydrophilic surface. Reprinted by permission from Macmillan Publishers Ltd: [*Nature*] (Wong et al.), copyright (2011)

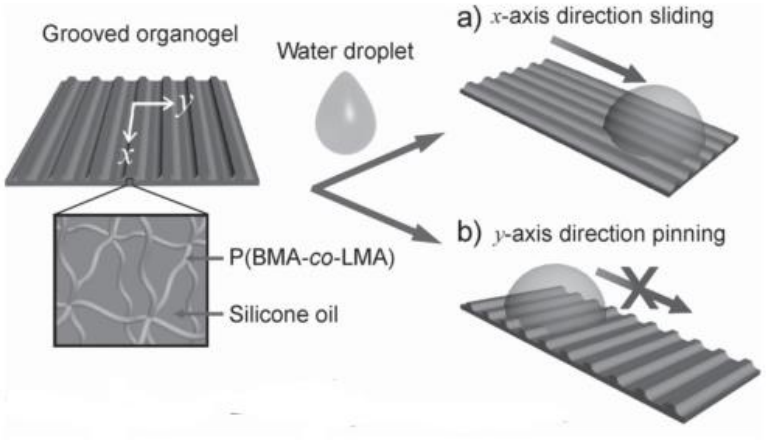

Figure 4: Illustration of the microgrooved organogel structure. Copyright (2014) WILEY-VCH Verlag GmbH & Co. KGaA , Weinheim. Used with permission from (Zhang et al., "Grooved Organogel Surfaces towards Anisotropic Sliding of Water Droplets," *Advanced Materials,* John Wiley and Sons)

The purpose of the work done in this thesis was to mimic and combine the natural mechanisms discussed above to create a surface coating that is directionally omniphobic. Essentially, the surface coating would be an ideal cross between the mechanisms of the butterfly wing and pitcher plant. While the butterfly wings could repel water directionally, the surface discussed further in this thesis aims to directionally repel a

variety of liquids by using a lubricant film to coat a grooved microstructure. Anisotropic directional surfaces are still a relatively novel idea that could have a large impact in energy and biomedical applications such as microprocessor cooling, hydropower turbines, and directional syringes (Hancock and Demirel). See Figure 5 for a visual representation of the combination of these mechanisms.

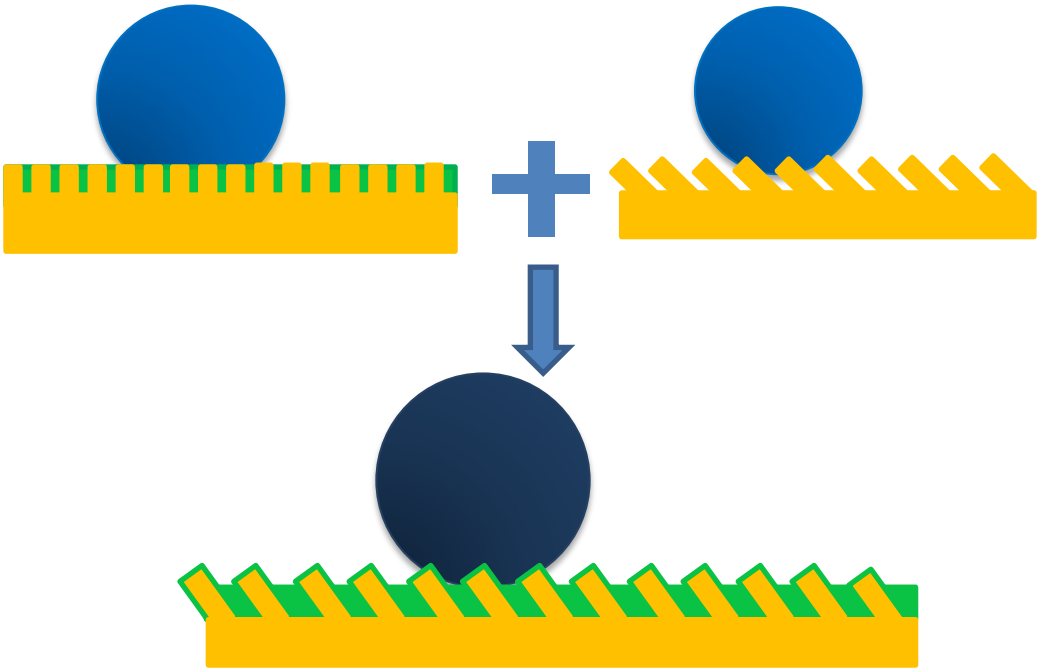

Figure 5: Illustration of the mechanisms of the pitcher plant (top left) and the butterfly wing (top right) combining to create a directionally omniphobic surface (bottom)

The surface created in this work was a cross between the SLIPS and microgrooved surfaces discussed above. Four microgrooved silicon wafers were created at varying groove widths (50, 100, 150, and 200 microns). Instead of using organogel and silicone oil to create the slippery surface, this surface was coated with Krytox 103 lubricant to create a thin film over the entire surface area. In this way, the hope was that this surface would be able to repel liquids of various surface tensions (pitcher plant and SLIPS) as well as repel the liquids directionally (butterfly and organogel surface).

The remainder of this thesis will outline the testing done on this directional SLIPS to determine its effectiveness in directionally repelling liquids of varying surface tension (water, hexadecane, and octane). It will then present the results of the experiments and discuss further what the results imply as to how well the directional SLIPS works. It will then comment on some possible future work to be done to better determine if the directional SLIPS works as expected.

Chapter 2

Experimental Setup

Materials and Equipment

DuPont Krytox 103 GPL Oil Lubricant, Hexadecane ($C_{16}H_{34}$), Octane (C_8H_{18}), Deionized Water, Structured Silicon Wafers (50, 100, 150, 200 µm with 30 µm groove depth), Air Displacement Micropipette, Inclinometer, Mituyuto IP67 Caliper, Mettler Toledo XP504DR Analytical Balance, Laurell Technologies Corporation WS-650MZ-23NPP Spin Coater

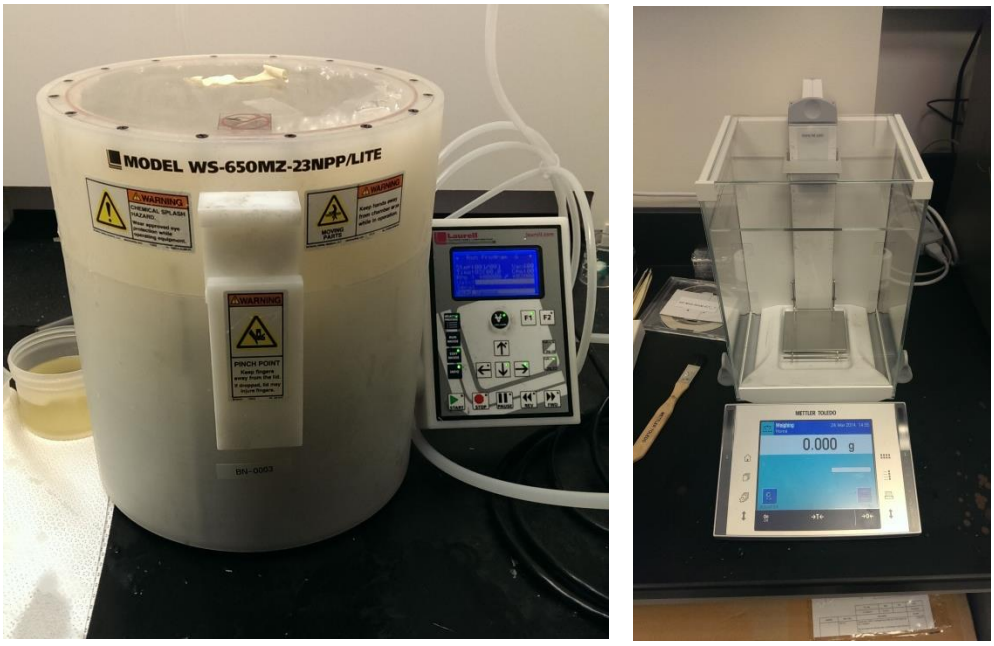

Figure 6: Laurel Technologies Coporation Spin Coater (left) and the Mettler Toledo Analytical Balance (right) used in testing

Basic Overview

The purpose of the following experiments was to test the ability of four silicon wafer samples of varying groove pitches to directionally repel three different liquid substances: deionized water, hexadecane, and octane. Each sample was first wetted with the Krytox 103 lubricant at different spin speeds to form a SLIPS. The inclinometer was then used to determine the sliding angle of the various liquids upon the surface of the SLIPS, both parallel and perpendicular to the run of the grooves. The data gathered could then be analyzed to determine the success of directional repellency based on the wafer groove size as well as the lubricant height (which is dependent upon the spin speed of the spin coater).

Determining Lubricant Height

The purpose of this first test was to first and foremost determine an acceptable range of spin speeds at which to coat the samples so that they were all sufficiently covered at least to the critical volume (discussed further below). This test also determined the height of the lubricant film on each sample at these various spin speeds. These lubricant heights would later be necessary to ascertain the effect the directional SLIPS has on repellency.

Before sliding angle data could be gathered, the height of the lubricant film on the samples needed to be calculated for the different spin speeds. To begin, the area of each silicon wafer sample was measured using the electronic caliper. Since none of the samples were cut into perfect rectangles, a bit of basic geometry was necessary to adequately estimate the area of each sample. The area calculations and diagrams can be

found in Appendix A. Before the coating process, the samples were placed in the Mettler Toledo analytical balance to measure the "dry" mass of each.

Next, one sample was placed into the Laurell Technologies Corporation spin coater and topped with a generous amount of Krytox lubricant, ensuring that the entire surface of the sample was covered. The spin coater was set to run for two minutes with the acceleration parameter set at 50. Testing began with a spin speed of 1000 RPM. After the spin cycle was completed, the "wet" mass of the coated silicon wafer sample was measured in the analytical balance. From there, the following equations were used to calculate the height of the lubricant on the sample.

$$V_{cr} = \frac{Ad}{2}$$

where V_{cr} *= critical lubricant volume (volume of lubricant needed to just fill the grooves)*

A *= sample area*

d *= groove depth (30µm for all samples)*

The factor of two in this equation is derived from the estimation that approximately half of the silicon wafer surface are the groove "valleys" that need to be filled with the Krytox lubricant.

$$\Delta W = W_c - W_o$$

where ΔW *= change in mass*

W_c *= coated mass (sample and lubricant)*

W_o *= initial mass of the sample*

$$\Delta V = \frac{\Delta W}{\rho}$$

where ΔV *= volume of lubricant added*

ρ *= mass density of Krytox 103 (1.92 g/mL)*

$$h = 2\frac{\Delta V}{A} \; for \; \Delta V \leq V_{cr}$$

$$h = d + \frac{\Delta V - V_{cr}}{A} \; for \; \Delta V > V_{cr}$$

where h *= height of the lubricant*

Again, the factor of two in the first of the two above equations is derived from the estimation that half of the wafer sample is fillable.

Next, the following equation was used to pinpoint a spin speed which corresponded to the critical volume of lubricant.

$$W_{cr} = \rho V_{cr} + W_o$$

where W_{cr} *= mass at which the sample has been coated with the critical volume of lubricant*

When the "wet" mass of the sample matched or nearly matched this critical mass, the spin speed for that particular run would represent a cutoff spin speed at which lower speeds wouldn't need to be tested (since the lubricant is already fully filling the grooves and would produce a sliding angle difference of 0°, as discussed further in the next section). After a fair amount of trial and error in finding cutoff weights for all four samples, each wafer was coated and measured for pertinent data at the following spin

speeds: 550 RPM, 600 RPM, 800 RPM, 900 RPM, 1000 RPM, 2000 RPM, 3000 RPM, 4000 RPM, 5000 RPM, 6000 RPM, 7000 RPM, and 8000 RPM.

Obtaining Sliding Angle Data

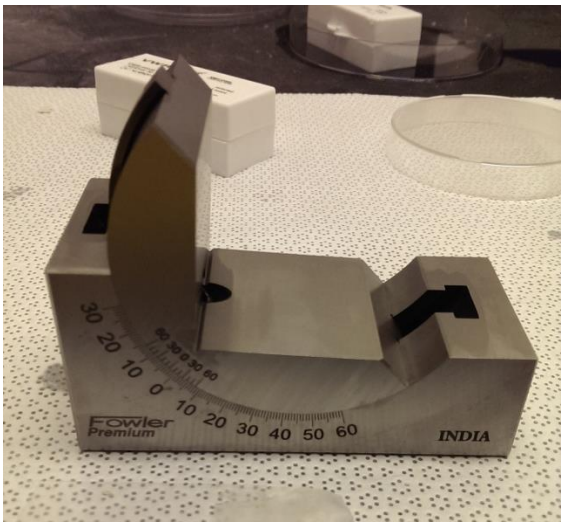

Figure 7: Inclinometer used to measure sliding angle

The purpose of the sliding angle test was to obtain the raw data with which the corresponding lubricant height data could be plotted against. The fundamental idea behind this test is that the liquid droplet's motion on the inclinometer would be directly affected by the direction of the silicon wafer grooves. In particular, at lower lubricant heights, it was expected that the droplet's motion would be impeded by a groove orientation perpendicular to the slide. The angles at which the droplets fall for both orientations were recorded for all the different speeds and samples.

Starting from the lowest spin speed (550 RPM), a Krytox 103 coating was reapplied to the silicon wafer sample using the spin coater. The sample was then placed

on the inclinometer at an initial angle of 0° with the grooves first running parallel with the tilt. With the micropipette set to a volume of 15 μL, a drop of deionized water was transferred onto the sample. The inclinometer was then slowly adjusted until the droplet began to slide down on the surface of the sample. The angle at which this occurred was then recorded. This process was repeated for a total of five data points for the parallel setup. Care was taken to ensure that the droplets had varying starting points on the sample to promote diversification of the data. After all the parallel data points had been collected, the silicon sample was then rotated 90° so that the grooves ran perpendicular to the tilt. Another five data points were taken in this setup using the same process as delineated above. The sample was then cleaned off and placed back into the spin coater, and coated again with the lubricant at the same spin speed. This time, five data points for both parallel and perpendicular groove orientation were gathered for hexadecane droplets instead of deionized water. By the same method, five data points for parallel and perpendicular orientation were also obtained for octane droplets.

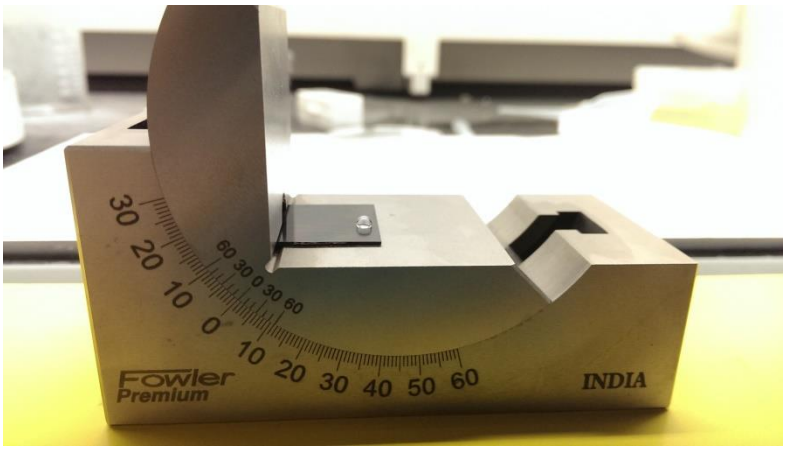

Figure 8: 50 micron sample with a droplet of water on top. Notice the very round shape of the droplet due to its high surface tension

Figure 9: Droplets of octane on the 50 micron sample. Notice the shape adhering somewhat tightly to the groove geometry due to octane's low surface tension

After obtaining all the sliding angle data for 550 RPM, this data collection process was repeated for the remaining eleven spin speeds for all four samples. It is important to note that because octane and hexadecane have relatively low surface tensions, at the higher spin speeds (lower lubricant height), it became slightly harder to remove all of the liquid droplets completely from the sample surface. Therefore, it became necessary to wash off the sample surface with deionized water from the lab sinks to ensure a clean surface for further lubricant coatings. Separate pipette tips were also used for the three different liquids to avoid cross contamination.

Chapter 3

Results

After obtaining the raw data in the lubricant height experiment, it was very simple to organize the data and the calculations into tables. All calculations were done using the equations outlined in the previous chapter. From there, the calculated height of the lubricant for each sample was plotted against the spin speed at which that lubricant height was produced. The results can be seen below in Figure 10. The full lubricant height tables can all be found in Appendix B, while the condensed data can be found below in Table 1.

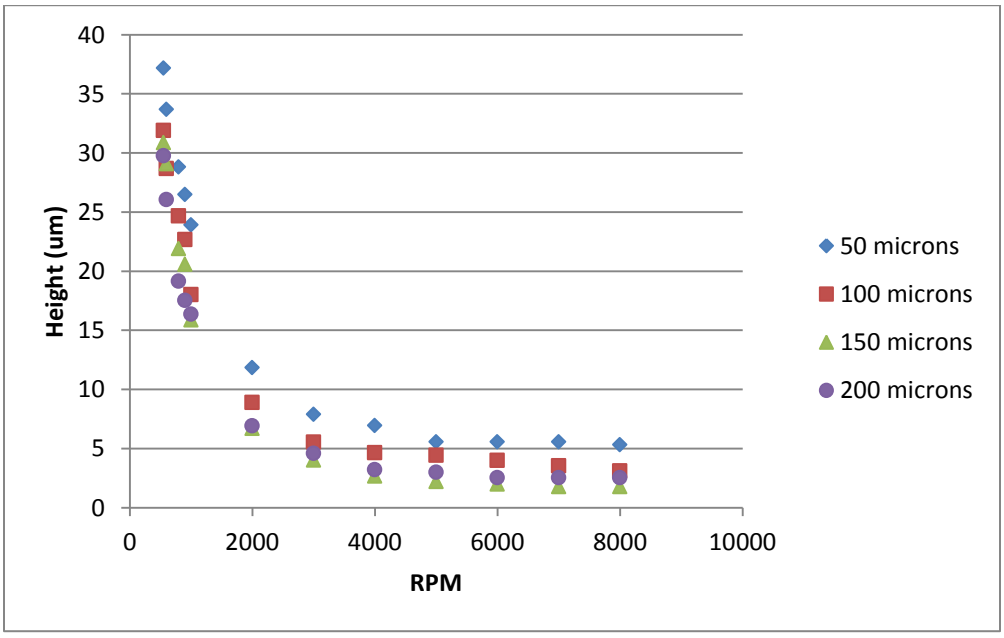

Figure 10: Lubricant Height vs. Spin Speed in RPM for all four grooved samples

Table 1: Lubricant height data for all spin speeds and all samples, where p denotes groove pitch of the sample

Lubricant Height (μm)				
Spin Speed	**p=50 μm**	**p=100 μm**	**p=150 μm**	**p=200 μm**
550	37.2	31.9	30.9	29.8
600	33.7	28.7	29.1	26.1
800	28.8	24.7	21.9	19.2
900	26.5	22.7	20.6	17.5
1000	23.9	18.0	15.9	16.4
2000	11.9	8.9	6.7	6.9
3000	7.9	5.6	4.0	4.6
4000	7.0	4.7	2.7	3.2
5000	5.6	4.4	2.2	3.0
6000	5.6	4.0	2.0	2.5
7000	5.6	3.6	1.8	2.5
8000	5.3	3.1	1.8	2.5

After completing the sliding angle experiment (raw data found in Appendix C), the raw data was then manipulated into a more meaningful format. Since the purpose of these experiments was to test the ability of the SLIPS surface to directionally repel liquids based on lubricant height (essentially parallel versus perpendicular orientation), the sliding angle difference between parallel and perpendicular orientations carried more meaning than the raw data itself. Here, the sliding angle difference is defined as:

$$\alpha = \theta_{perpindcular} - \theta_{parallel}$$

where α = *sliding angle difference*

θ = *sliding angle*

After calculating the sliding angle difference for each sample, the average sliding angle difference as well as the variance of the data was calculated for each speed. This data can be found in Appendix D. Combining the sets of data from both experiments, the average value of sliding angle difference for each spin speed was plotted against the corresponding value of lubricant height to get a representation of how the lubricant height effects the directional repellency of the different silicon wafer samples. The four plots can be found below in Figures 11 - 14. The sliding angle difference data points in the following plots were the mean sliding angle differences of the five collected data points for each individual spin speed.

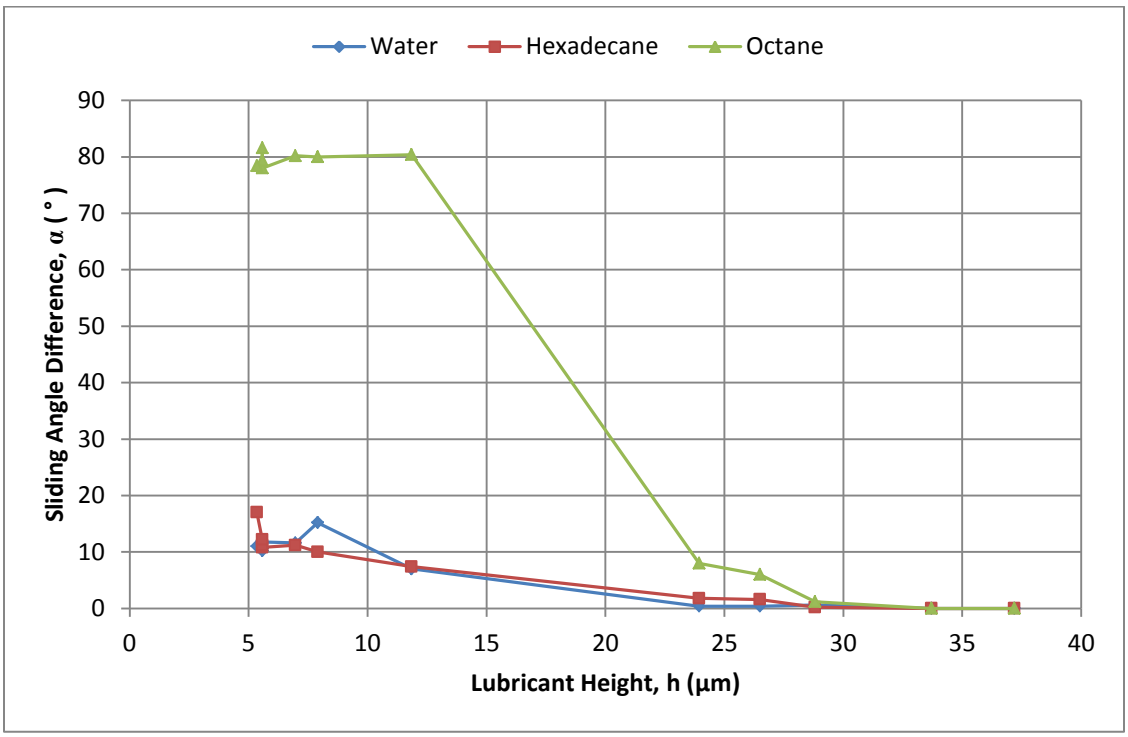

Figure 11: Sliding Angle Difference vs. Lubricant Height, 50 micron sample

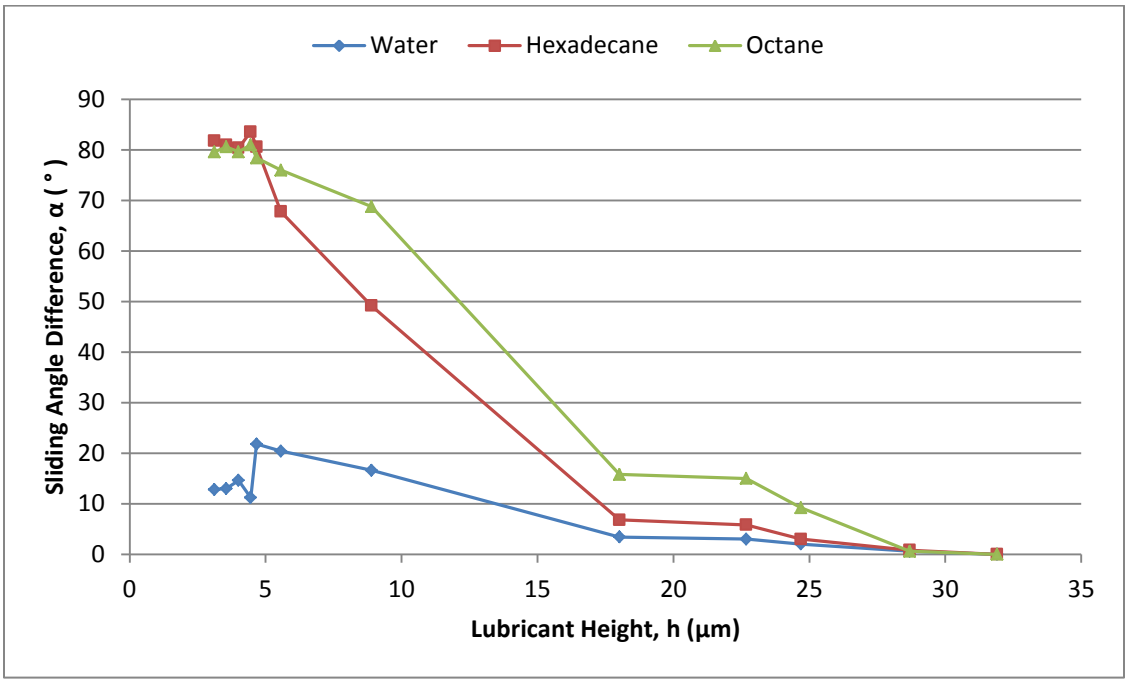

Figure 12: Sliding Angle Difference vs. Lubricant Height, 100 micron sample

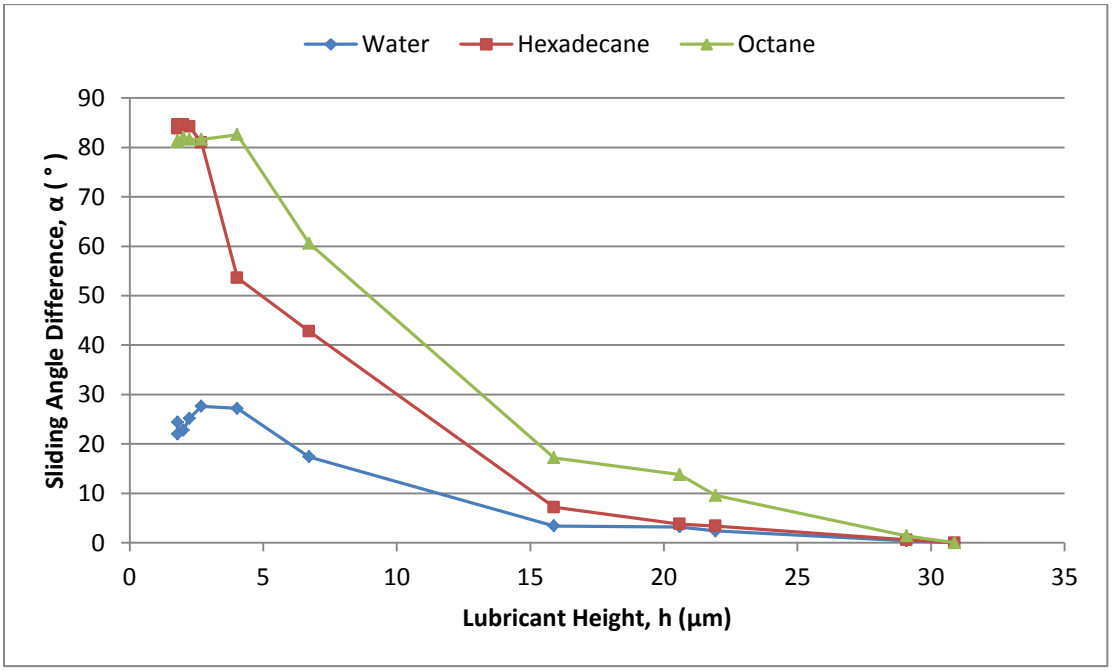

Figure 13: Sliding Angle Difference vs. Lubricant Height, 150 micron sample

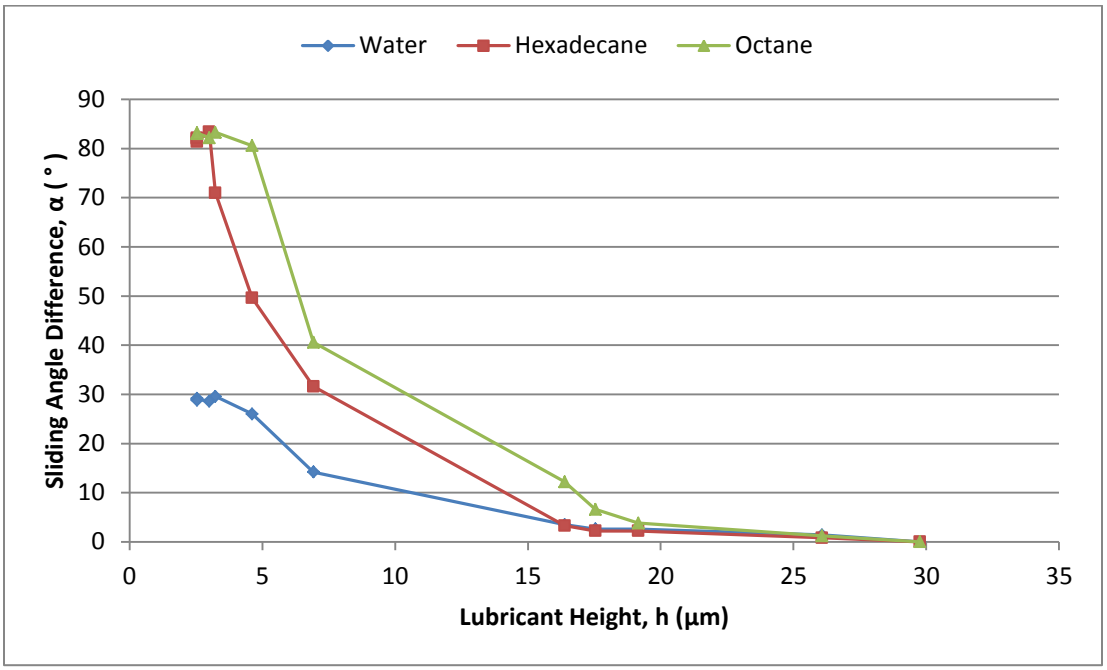

Figure 14: Sliding Angle Difference vs. Lubricant Height, 200 micron sample

Note that the bunching of data points around the 80 – 90 degree area is due to the fact that no data points were recorded past 90°. If the droplet did not fall at all during sliding angle testing, its sliding angle was simply recorded as 90°. Thus, at low lubricant heights, the octane and hexadecane began to resist sliding entirely, and the same recording of 90° was used for all of them.

Chapter 4

Discussion and Conclusions

Discussion of Results

For the most part, the three test liquids behaved essentially as expected under the different test conditions. To get a better understanding of the phenomena in this experiment, one must first examine the surface tensions of the liquids, as outlined in Table 2 below.

Table 2: Surface tensions of test liquids

Test Liquid	*Surface Tension (20° C, in mN/m)*
Water	72.80
Hexadecane	27.47
Octane	21.62

It is easy to tell that while hexadecane and octane share a relatively similar value of surface tension, water exhibits a much greater value than either. A higher surface tension value leads to a smaller contact area between the wafer and the droplet due to higher cohesive forces in the droplet. Thus, when the water droplet is placed on the grooved surface, its high surface tension forms a sort of air cushion within the grooves. In this way, the water droplet sits more entirely on the surface than in the grooves

themselves, which leads to a smaller sliding angle difference between the parallel and perpendicular orientations as the droplet is not impeded well by the groove depth.

Octane and hexadecane, on the other hand, have surface tension values of roughly one third the value of water. These low surface tension values mean that the octane and hexadecane droplets spread out more into the grooves and have a higher contact area with the surface. This increased contact significantly impedes the droplet's motion in the perpendicular orientation.

With all this in mind, Figures 11 - 14 from Chapter 3 exhibit expected behavior from the three liquids. The water, having a high surface tension, shows a relative trend of increasing sliding angle difference with lower lubricant height (meaning more contact area), but remains a significant amount lower than the sliding angle differences measured for hexadecane and octane. The other two liquids also show an inverse trend between lubricant height and sliding angle difference. It makes sense that the hexadecane and octane data points are closer together than the water based on surface tension. Effectively, for the 100 – 200 micron groove width samples, the testing concluded that the directional SLIPS developed with the silicon samples and Krytox 103 proved to be effective in at least impeding, and in some cases completely hindering, the motion of droplets and that lubricant height has a direct effect on this impedance.

However, when looking at the data for the 50 micron sample, some significant discrepancies are immediately apparent. First, there seems to be a rather sudden jump from small to large sliding angle difference when testing the octane droplets. As can be seen in Figure 11, the sliding angle difference jumps from roughly 8° to 80° after just one change in spin speed of 1000 RPM. This large and sudden change may not look as

disconcerting, however, if there were simply more data points taken to smooth out the curve; namely, if more spin speeds between 1000 and 2000 RPM were tested. Thus, with that in mind, the seemingly large jump in the octane data may not be so much an error as a plot in need of more data points.

There is, however, another problem with the data of the 50 micron sample. The hexadecane data shares much more similarity to water than to octane. Instinctively, one would expect the hexadecane data to match much better with the octane based on surface tension. As to figuring out why this phenomenon occurred is beyond the scope of this thesis, as more research would need to be done. However, a possible hypothesis and approach to explaining this is described below.

Future Work

One conceivable reason that the hexadecane sliding angle data shared a striking resemblance to the water data on the 50 micron sample is that an air cushion still existed between the lubricant and the hexadecane within the groove structure. This would imply that for some value of surface tension in between the values of 21.62 mN/m and 27.47 mN/m for octane and hexadecane, respectively, the wetting of test liquid into the 50 micron grooves is not complete.

To test this hypothesis, one must first understand the modeling of wetting. First, the Wenzel model of wetting (Figure 15) is defined by the following equation:

$$\cos\theta^* = r\cos\theta_Y$$

where θ^* *= apparent contact angle at equilibrium*

θ_Y = *Young contact angle for an ideal surface***

r = *roughness ratio (true area of surface/apparent area)*

** note that θ_Y is a function of advancing contact angle and receding contact angle (see Figure 16), the equation for which will not be listed here as it is unnecessary for this general discussion.

The Cassie-Baxter model (Figure 15) is defined by the following equation:

$$\cos\theta^* = r_f f cos\theta_Y + f - 1$$

where r_f = *wet surface area roughness ratio*

f = *fraction of surface area wet by the liquid*

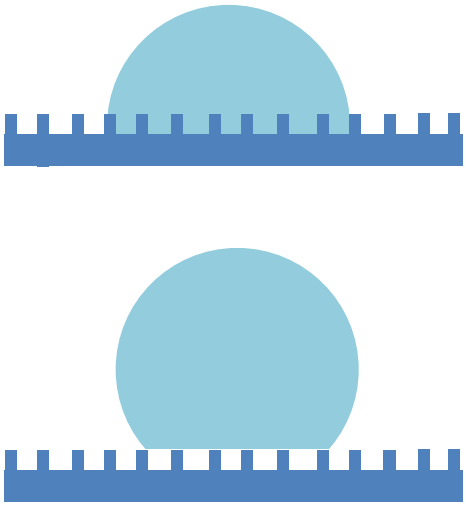

Figure 15: The Wenzel Model (top) and the Cassie-Baxter Model (bottom)

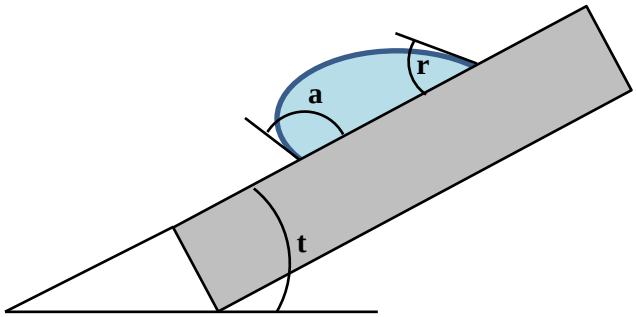

Figure 16: Illustration of the advancing (a) and receding (r) contact angles for a droplet in tilt (angle t)

The Wenzel model assumes that as the contact line progresses on the solid surface, the liquid completely wets and conforms to the topological variations in the surface. The Cassie-Baxter model assumes that air pockets are formed beneath the liquid and solid surface in the grooves, so that the droplet essentially does not fill the grooves at all (Quéré). In reality, the problem faced in this test would lie somewhere in between the two models, as some sliding angle difference was recorded and the droplet can therefore not be experiencing a fully Cassie regime.

The main point to grasp here is that for either of these equations, the apparent contact angle at equilibrium, or θ^*, increases as the groove width becomes smaller. This is because as the groove widths become smaller, more grooves will be present on a set size of silicon wafer. With more grooves comes more total surface area of the wafer. As the actual surface area of the wafer gets larger, so does the roughness ratio. Higher values of

r and r_f lead the right side of both of the above equations to go up; thus, the corresponding value of θ^* must also increase. As can be seen in Figure 15, higher values in contact angle correspond to droplets more or less sitting on top of the grooved structure with air pockets below them. This leads to lower values of sliding angle difference, as exhibited by the hexadecane droplets on the 50 micron silicon sample.

To test if this hypothesis is correct, experiments could be carried out with silicon wafers of groove widths even less than 50 microns. One would expect to see that at a small enough groove width, the octane would begin to behave more like the water with lower values of sliding angle difference due to the increase in contact angle. If this is proven to be the case, the discrepancy in the data for the 50 micron sample would be accounted for and not deemed as error.

Conclusions

Overall, the SLIPS created with the engineered silicon microstructure and Krytox 103 lubricant exhibited a significant ability to induce directional omniphobic behavior based on the three test liquids used. This difference is best seen at higher spin coating speeds (corresponding to low lubricant height) and wider groove dimensions. As discussed, if the groove width becomes too small, the contact angle of the droplet becomes too large and directional repellency is not as pronounced. Preliminarily, these tests have shown that this surface coating at least deserves to be considered in the development of a directionally omniphobic coating. It would do a great deal of good to first test smaller groove samples to determine whether or not the contact angle hypothesis

bears any weight. If it is so, the discrepancy in the raw data would become avoidable. More research has to be done to verify and properly quantify the surface's effectiveness, but the foundation has been set with the experiments completed and data collected here.

Appendix A

Area Calculations

50 µm sample

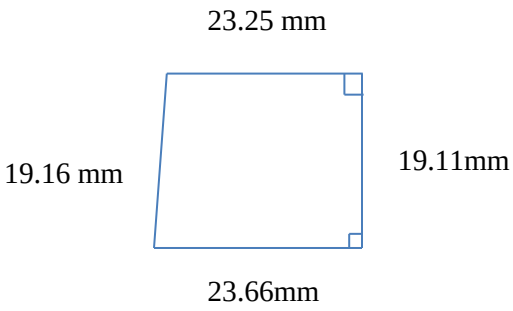

$$A \cong \frac{23.25\ mm + 23.66\ mm}{2}(19.11\ mm)$$

$$A \cong 448.2\ mm^2$$

Figure 17: 50 micron sample area

100 µm sample

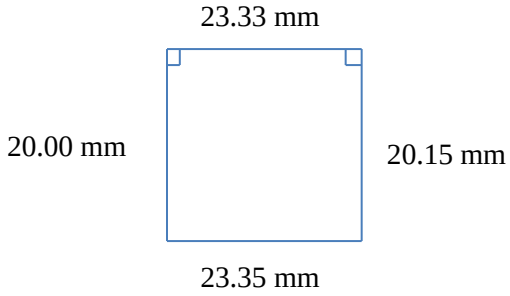

$$A \cong \frac{20.00\ mm + 20.15\ mm}{2}(23.33\ mm)$$

$$A \cong 468.4\ mm^2$$

Figure 18: 100 micron sample area

150 µm sample

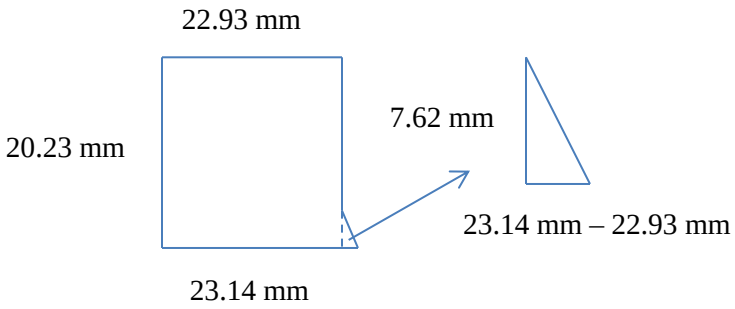

Figure 19: 150 micron sample area

$$\boldsymbol{A \cong (22.93\ mm)(20.23\ mm) + \frac{23.14\ mm - 22.93\ mm}{2}(7.62\ mm)}$$

$$\boldsymbol{A \cong 464.7\ mm^2}$$

200 µm sample

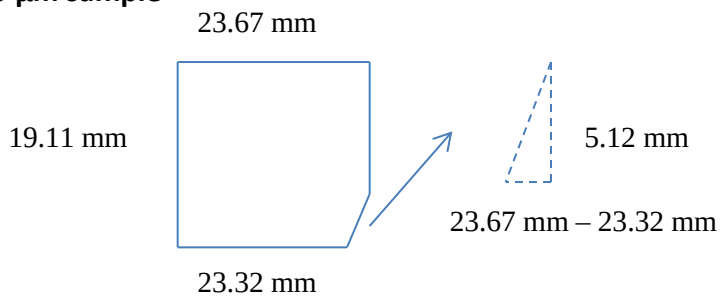

Figure 20: 200 micron sample area

$$\boldsymbol{A \cong (23.67\ mm)(19.11\ mm) - \frac{23.67\ mm - 23.32\ mm}{2}(5.12\ mm)}$$

$$\boldsymbol{A \cong 451.4\ mm^2}$$

Appendix B

Lubricant Height Data

Table 3: 50 microns, lubricant height

50 microns		cutoff weight (g)	0.5018	
W0 (g)	0.4889			
Area (um^2)	4.5E+08			
Vcr (um^3)	6.7E+09			
RPM	Wc (g)	ΔW (g)	ΔV (um^3)	h (um)
550	0.508	0.0191	9.9E+09	37.2
600	0.505	0.0161	8.4E+09	33.7
800	0.5013	0.0124	6.5E+09	28.8
900	0.5003	0.0114	5.9E+09	26.5
1000	0.4992	0.0103	5.4E+09	23.9
2000	0.494	0.0051	2.7E+09	11.9
3000	0.4923	0.0034	1.8E+09	7.9
4000	0.4919	0.003	1.6E+09	7.0
5000	0.4913	0.0024	1.3E+09	5.6
6000	0.4913	0.0024	1.3E+09	5.6
7000	0.4913	0.0024	1.3E+09	5.6
8000	0.4912	0.0023	1.2E+09	5.3

Table 4: 100 microns, lubricant height

100 microns		cutoff weight (g)	0.5423	
W0 (g)	0.5288			
Area (um^2)	4.7E+08			
Vcr (um^3)	7.0E+09			
RPM	Wc (g)	ΔW (g)	ΔV (um^3)	h (um)
550	0.544	0.0152	7.9E+09	31.9
600	0.5417	0.0129	6.7E+09	28.7
800	0.5399	0.0111	5.8E+09	24.7
900	0.539	0.0102	5.3E+09	22.7
1000	0.5369	0.0081	4.2E+09	18.0
2000	0.5328	0.004	2.1E+09	8.9
3000	0.5313	0.0025	1.3E+09	5.6
4000	0.5309	0.0021	1.1E+09	4.7
5000	0.5308	0.002	1.0E+09	4.4
6000	0.5306	0.0018	9.4E+08	4.0
7000	0.5304	0.0016	8.3E+08	3.6
8000	0.5302	0.0014	7.3E+08	3.1

Table 5: 150 microns, lubricant height

150 microns		cutoff weight (g)	0.5342	
W0 (g)	0.5208			
Area (um^2)	4.7E+08			
Vcr (um^3)	7.0E+09			
RPM	Wc (g)	ΔW (g)	ΔV (um^3)	h (um)
550	0.535	0.0142	7.4E+09	30.9
600	0.5338	0.013	6.8E+09	29.1
800	0.5306	0.0098	5.1E+09	21.9
900	0.53	0.0092	4.8E+09	20.6
1000	0.5279	0.0071	3.7E+09	15.9
2000	0.5238	0.003	1.6E+09	6.7
3000	0.5226	0.0018	9.4E+08	4.0
4000	0.522	0.0012	6.2E+08	2.7
5000	0.5218	0.001	5.2E+08	2.2
6000	0.5217	0.0009	4.7E+08	2.0
7000	0.5216	0.0008	4.2E+08	1.8
8000	0.5216	0.0008	4.2E+08	1.8

Table 6: 200 microns, lubricant height

200 microns		cutoff weight (g)	0.5194	
W0 (g)	0.5064			
Area (um^2)	4.5E+08			
Vcr (um^3)	6.8E+09			
RPM	Wc (g)	ΔW (g)	ΔV (um^3)	h (um)
550	0.5193	0.0129	6.7E+09	29.8
600	0.5177	0.0113	5.9E+09	26.1
800	0.5147	0.0083	4.3E+09	19.2
900	0.514	0.0076	4.0E+09	17.5
1000	0.5135	0.0071	3.7E+09	16.4
2000	0.5094	0.003	1.6E+09	6.9
3000	0.5084	0.002	1.0E+09	4.6
4000	0.5078	0.0014	7.3E+08	3.2
5000	0.5077	0.0013	6.8E+08	3.0
6000	0.5075	0.0011	5.7E+08	2.5
7000	0.5075	0.0011	5.7E+08	2.5
8000	0.5075	0.0011	5.7E+08	2.5

Appendix C

Sliding Angle Raw Data

Table 7: Sliding angle data, 50 microns

50 µm					
Water		Hexadecane		Octane	
Parallel	Perp	Parallel	Perp	Parallel	Perp
550 RPM					
4	4	4	4	5	5
5	5	5	5	5	5
5	5	5	5	5	5
5	5	4	4	5	5
5	5	4	4	5	5
600 RPM					
5	5	5	5	5	5
5	5	5	5	7	7
5	5	4	4	6	6
5	5	4	4	6	6
5	5	4	4	6	6
800 RPM					
5	6	4	5	7	7
5	6	6	6	7	9
5	5	5	5	9	10
6	6	5	5	10	12
5	6	5	5	11	12
900 RPM					
6	6	6	7	8	15
7	8	6	8	9	16
5	6	5	7	7	14
6	6	6	7	7	13
6	6	5	7	8	11

1000 RPM					
5	5	5	7	8	14
5	6	5	7	8	17
6	6	6	7	9	18
6	7	6	8	10	18
5	5	6	8	9	17
2000 RPM					
12	18	9	18	8	90
12	19	8	14	9	90
12	19	10	14	9	90
12	20	8	20	12	90
12	19	9	15	10	90
3000 RPM					
8	24	7	19	8	90
18	36	7	19	12	90
17	33	7	18	13	90
10	23	8	14	8	90
14	27	8	17	9	90
4000 RPM					
9	19	8	18	8	90
10	20	8	23	10	90
8	22	8	19	10	90
12	23	8	19	7	90
12	25	9	18	12	88
5000 RPM					
7	17	7	20	8	88
7	17	7	20	10	84
7	21	9	18	11	90
9	24	13	22	11	90
9	19	10	20	12	90
6000 RPM					
10	16	8	18	8	90
10	20	8	18	8	90
9	22	10	23	8	90
13	25	7	20	9	90
9	19	13	23	9	90
7000 RPM					
8	18	9	20	7	90
8	20	9	22	12	90
8	23	11	24	12	90
10	20	14	23	9	90
14	20	10	25	13	90
8000 RPM					
9	17	8	23	12	90
9	20	8	25	12	90
10	21	8	28	15	90
10	24	12	26	9	90
11	22	10	29	10	90

Table 8: Sliding angle data, 100 microns

100 µm					
Water		Hexadecane		Octane	
Parallel	Perp	Parallel	Perp	Parallel	Perp
550 RPM					
4	4	3	3	4	4
4	4	3	3	4	4
4	4	4	4	3	3
4	4	3	3	3	3
4	4	3	3	4	4
600 RPM					
5	5	3	4	4	4
5	6	4	5	4	5
4	5	4	5	4	4
5	5	4	5	4	5
5	6	4	4	4	5
800 RPM					
5	7	4	8	6	19
6	7	5	8	6	15
5	8	7	10	7	15
6	8	4	6	6	16
5	7	5	8	7	13
900 RPM					
5	9	6	12	6	21
5	9	5	11	6	22
5	7	5	11	7	20
6	9	6	11	6	24
6	8	5	11	8	21
1000 RPM					
6	10	4	14	8	28
7	10	4	14	10	24
7	10	7	13	9	25
8	11	8	11	7.5	22
8	12	5	10	7.5	22

2000 RPM					
7	25	4	55	6	76
7	25	4	57	7	80
9	24	5	51	9	78
7	23	5	53	8	75
8	24	6	54	8	73
3000 RPM					
7	27	4	75	10	85
7	28	4	73	10	90
7	27	7	77	15	90
9	30	6	70	11	83
10	30	6	71	12	90
4000 RPM					
9	30	7	86	10	90
10	34	7	88	10	90
11	29	6	90	10	90
6	30	9	86	11	85
9	31	8	90	12	90
5000 RPM					
6	16	6	90	6	90
6	16	6	90	9	90
7	16	6	90	10	90
7	18	8	90	10	90
6	22	6	90	10	90
6000 RPM					
6	25	9	90	10	90
6	20	8	90	10	90
7	20	9	90	10	90
6	19	10	90	11	90
7	21	12	90	11	90
7000 RPM					
5	18	7	90	9	90
6	18	7	90	9	90
7	20	8	90	9	90
6	19	11	90	10	90
6	20	12	90	10	90
8000 RPM					
6	18	7	90	10	90
6	20	7	90	10	90
6	19	10	90	11	90
5	18	9	90	10	90
6	18	8	90	11	90

Table 9: Sliding angle data, 150 microns

150 µm					
Water		Hexadecane		Octane	
Parallel	Perp	Parallel	Perp	Parallel	Perp
550 RPM					
4	4	3	3	4	4
4	4	4	4	4	4
5	5	3	3	3	3
4	4	4	4	3	3
4	4	4	4	3	3
600 RPM					
4	5	4	4	3	5
5	5	4	4	3	5
5	5	3	4	4	5
5	6	3	4	4	5
5	5	4	5	4	5
800 RPM					
4	6	4	7	4	15
4	6	4	7	4	15
4	6	4	7	5	12
4	7	4	8	4	13
4	7	4	8	4	14
900 RPM					
4	8	4	7	4	17
4	8	4	8	4	18
5	7	5	9	5	21
5	8	5	9	5	20
4	7	4	8	5	16
1000 RPM					
4	8	5	11	4	21
4	8	5	12	4	22
5	9	5	12	6	25
5	8	4	12	5	24
6	8	4	12	5	18

2000 RPM					
5	22	6	49	6	65
5	22	6	50	6	65
5	21	6	50	7	69
6	24	7	51	6	67
6	25	7	46	6	68
3000 RPM					
9	40	6	60	6	90
11	40	6	59	8	90
11	35	6	58	9	90
10	37	6	61	7	90
11	36	6	60	7	90
4000 RPM					
7	38	5	90	8	90
9	37	5	86	8	90
9	39	6	86	10	90
11	34	5	84	8	90
9	35	5	85	8	90
5000 RPM					
6	26	5	90	7	90
6	31	5	87	10	90
8	33	5	90	10	90
10	38	6	90	7	90
10	38	5	90	8	90
6000 RPM					
5	25	5	90	7	90
6	28	5	90	7	90
7	30	5	90	11	90
6	27	6	90	7	90
7	35	6	90	8	90
7000 RPM					
7	28	6	90	9	90
7	33	6	90	9	90
8	31	6	90	9	90
7	25	7	90	8	90
8	30	6	90	9	90
8000 RPM					
6	28	5	90	9	90
9	35	5	90	8	90
10	35	5	90	8	90
6	26	6	90	9	90
8	37	6	90	9	90

Table 10: Sliding angle data, 200 microns

200 µm					
Water		Hexadecane		Octane	
Parallel	Perp	Parallel	Perp	Parallel	Perp
550 RPM					
3	3	4	4	3	3
4	4	4	4	3	3
4	4	3	3	4	4
4	4	4	4	4	4
3	3	3	3	4	4
600 RPM					
4	5	3	4	4	5
4	5	3	4	4	5
3	5	4	5	3	5
3	5	4	4	4	5
4	5	3	4	4	5
800 RPM					
4	7	3	5	3	7
4	7	3	6	3	7
4	6	4	6	3	7
3.5	6	4	6	3	6
3.5	6	5	7	3	7
900 RPM					
4	6	4	6	4	10
4	7	4	7	4	11
4	6	4	5	4	11
4	7	4	7	4	11
3	6	4	6	4	10
1000 RPM					
4	7.5	3	6.5	3.5	15
4	7	4	7	3.5	13
4	8	5	7	4	18
4	7	2	6	4	14
4	8	3	7	4	20

2000 RPM					
4	19	3	32	4	44
4	20	3	35	4	43
5	18	4	40	6	49
4	18	4	32	5	42
6	19	3	36	6	50
3000 RPM					
7	31	4	52	8	90
7	37	4	53	7	86
4	30	4	58	6	84
5	32	4	50	6	85
6	29	4	55	5	90
4000 RPM					
5	38	4	74	6	90
7	35	5	72	7	90
8	38	4	76	7	90
5	34	3	78	5.5	90
7	35	4	75	8	90
5000 RPM					
8	35	4	85	7	90
8	36	4	83	7	90
10	40	4	90	10	90
7	36	4	90	7	90
9	38	5	90	8	90
6000 RPM					
6	36	5	81	7	90
8	37	5	85	7	90
12	37	5	90	7	90
6	38	5	89	7	90
10	39	5	90	6	90
7000 RPM					
5	34	5	90	7	90
5	36	5	80	6	90
7	37	6	90	7	90
6	38	5	84	8	90
6	30	6	90	7	90
8000 RPM					
5	31	5	82	7	90
5	33	5	90	7	90
5	35	6	90	6	90
6	34	5	90	8	90
6	38	5	85	7	90

Appendix D

Average Sliding Angle Difference and Variance

Table 11: 50 micron sample difference and variance

50 um	Water		Hexadecane		Octane	
	Difference	var	Difference	var	Difference	var
550	0	0	0	0	0	0
600	0	0	0	0	0	0
800	0.6	0.3	0.2	0.2	1.2	0.7
900	0.4	0.3	1.6	0.3	6	3
1000	0.4	0.3	1.8	0.2	8	1.5
2000	7	0.5	7.4	9.8	80.4	2.3
3000	15.2	4.7	10	6.5	80	5.5
4000	11.6	3.3	11.2	5.2	80.2	7.2
5000	11.8	6.2	10.8	4.2	78	5.5
6000	10.2	7.2	11.2	2.7	81.6	0.3
7000	10.6	10.8	12.2	5.2	79.4	6.3
8000	11	4.5	17	6.5	78.4	5.3

Table 12: 100 micron sample difference and variance

100 um	Water		Hexadecane		Octane	
	Difference	var	Difference	var	Difference	var
550	0	0	0	0	0	0
600	0.6	0.3	0.8	0.2	0.6	0.3
800	2	0.4	3	0.5	9.2	6.7
900	3	1	5.8	0.2	15	4.5
1000	3.4	0.3	6.8	9.7	15.8	6.1
2000	16.6	1.8	49.2	7.7	68.8	9.2
3000	20.4	0.3	67.8	9.7	76	9.5
4000	21.8	6.2	80.6	7.3	78.4	6.8
5000	11.2	7.7	83.6	0.8	81	3
6000	14.6	6.3	80.4	2.3	79.6	0.3
7000	13	0.5	81	5.5	80.6	0.3
8000	12.8	0.7	81.8	1.7	79.6	0.3

Table 13: 150 micron sample difference and variance

150 um	Water		Hexadecane		Octane	
	Difference	var	Difference	var	Difference	var
550	0	0	0	0	0	0
600	0.4	0.3	0.6	0.3	1.4	0.3
800	2.4	0.3	3.4	0.3	9.6	2.8
900	3.2	0.7	3.8	0.2	13.8	3.7
1000	3.4	0.8	7.2	0.7	17.2	6.2
2000	17.4	1.3	42.8	4.7	60.6	2.3
3000	27.2	8.2	53.6	1.3	82.6	1.3
4000	27.6	10.3	81	5.5	81.6	0.8
5000	25.2	10.7	84.2	1.7	81.6	2.3
6000	22.8	9.7	84.6	0.3	82	3
7000	22	8.5	83.8	0.2	81.2	0.2
8000	24.4	12.3	84.6	0.3	81.4	0.3

Table 14: 200 micron sample difference and variance

200 um	Water		Hexadecane		Octane	
	Difference	var	Difference	var	Difference	var
550	0	0	0		0	0
600	1.4	0.3	0.8	0.2	1.2	0.2
800	2.6	0.18	2.2	0.2	3.8	0.2
900	2.6	0.3	2.2	0.7	6.6	0.3
1000	3.5	0.3	3.3	0.7	12.2	7.6
2000	14.2	1.7	31.6	10.3	40.6	8.3
3000	26	7.5	49.6	9.3	80.6	8.3
4000	29.6	4.3	71	8.5	83.3	1
5000	28.6	1.3	83.4	10.3	82.2	1.7
6000	29	6.5	82	15.5	83.2	0.2
7000	29.2	9.7	81.4	18.3	83	0.5
8000	28.8	5.2	82.2	12.7	83	0.5

REFERENCES

Hancock, Matthew J., and Melik C. Demirel. "Anisotropic Wetting on Structured Surfaces." *MRS Bulletin* 38.05 (2013): 391–396. Web. 22 Mar. 2014.

Ju, Jie et al. "A Multi-Structural and Multi-Functional Integrated Fog Collection System in Cactus." *Nature communications* 3 (2012): 1247. Web. 23 Mar. 2014.

Quéré, David. "Wetting and Roughness." *Annual Review of Materials Research* 38.1 (2008): 71–99. Web. 20 Mar. 2014.

Scholz, I et al. "Slippery Surfaces of Pitcher Plants: Nepenthes Wax Crystals Minimize Insect Attachment via Microscopic Surface Roughness." *The Journal of experimental biology* 213.Pt 7 (2010): 1115–25. Web. 30 Mar. 2014.

Wong, Tak-Sing et al. "Bioinspired Self-Repairing Slippery Surfaces with Pressure-Stable Omniphobicity." *Nature* 477.7365 (2011): 443–7. Web. 20 Mar. 2014.

Zhang, Pengchao et al. "Grooved Organogel Surfaces towards Anisotropic Sliding of Water Droplets." *Advanced materials (Deerfield Beach, Fla.)* (2014): 1–5. Web. 30 Mar. 2014.

Zheng, Yongmei et al. "Directional Water Collection on Wetted Spider Silk." *Nature* 463.7281 (2010): 640–3. Web. 19 Mar. 2014.

Zheng, Yongmei, Xuefeng Gao, and Lei Jiang. "Directional Adhesion of Superhydrophobic Butterfly Wings." *Soft Matter* 3.2 (2007): 178. Web. 20 Mar. 2014.

ACADEMIC VITA

Jonathan W. Wang

jon.wang91@gmail.com

Education

B.S., Mechanical Engineering, 2014, The Pennsylvania State University, University Park, PA

Honors and Awards

- Paul Morrow Endowed Scholarship, The Pennsylvania State University College of Engineering, 2010
- Academic Excellence Scholarship, The Pennsylvania State University Schreyer Honors College, 2010
- Dean's List, all semesters 2010 - Present

Association Memberships/Activities

- The National Society of Collegiate Scholars, 2011 – Present
- The National Society of Leadership and Success, 2011 - Present

Professional Experience

- Research Intern, Air Liquide, May 2009 – July 2009
- Nuclear Engineering Temporary Shielding Intern, Naval Sea Systems Command, May 2012 – August 2012, May 2013 – August 2013

Professional Presentations

- Out-brief presentations at the Puget Sound Naval Shipyard regarding the improvement of shipyard methods of radiation dosimetry as well as the design and implementation of a support fixture for a new non-destructive testing device